ADVANCED SCIENCE Open Access
www.advancedscience.com

Semiconducting Open-Shell Radicals for Precise Tumor Activatable Phototheranostics

Jie Zhang, Haifen Luo, Wen Ma, Jingqi Lv, Bo Wang, Fengwei Sun, Weijie Chi, Zhuting Fang,* and Zhen Yang**

Semiconducting open-shell radicals (SORs) have promising potential for the development of phototheranostic agents, enabling tumor bioimaging and boosting tumorous reactive oxygen species (ROS). Herein, a new class of semiconducting perylene diimide (PDI), designated as PDI(Br)$_n$ with various numbers of bromine (Br) atoms modified on PDI's bay/ortho positions is reported. PDI(Br)$_n$ is demonstrated to transform into a radical anion, [PDI(Br)$_n$]$^{\bullet-}$, in a reducing solution, with a typical *g*-value of 2.0022. Specifically, [PDI(Br)$_{4/6}$]$^{\bullet-}$ is generated in the weakly reductive tumor-mimicking solution and exhibits high stability in air. Quantum chemical kinetic simulation and ultrafast femtosecond transient absorption spectroscopy indicate that [PDI(Br)$_6$]$^{\bullet-}$ has a low π–π stacking energy (0.35 eV), a fast electron transfer rate (192.4 ps) and energy gap of PDI(Br)$_6$ ($\Delta E_{S1,T1}$ = 1.307 eV, $\Delta E_{S1,T2}$ = 0.324 eV) respectively, which together result in excited-state charge transfer characters. The PDI(Br)$_6$ nanoparticle radicals, [PDI(Br)$_6$] NPs$^{\bullet-}$, specifically enable chemodynamic and type-I photodynamic ROS generation in tumors, including superoxide and hydroxyl radicals, which elicit immunogenic cell death effect. Also, [PDI(Br)$_6$] NPs$^{\bullet-}$ facilitate activatable bioimaging-guided therapy due to their photoacoustic signal at 808 nm and NIR-II emission at 1115 nm. The work paves the way for the design of SORs for precise cancer theranostics.

1. Introduction

Cancer phototheranostics, integrating photodiagnosis and phototherapy with the assistance of biophotonic agents, enables the treatment with noninvasiveness, spatial localization, and manipulability.[1–4] To achieve precision phototheranostics, the ideal photonic molecules are required to possess activatable optical and pharmacological "turn on" properties in response to the specific tumor microenvironment (TME), such as excessive glutathione (GSH), reactive oxygen species (ROS), cytochrome reductase, nitro-reductase, to achieve highly sensitive differentiation of tumor by precise imaging with enhanced optical imaging contrast, simultaneously provide highly efficient therapeutic efficacy with minimized side effects.[5–9] Type-I photodynamic therapy (Type-I PDT) as a promising approach has been explored for cancer phototheranostics, owing to the generation of photoinduced cytotoxic long-lived ROS, such as superoxide radicals ($O_2^{\bullet-}$) and hydroxyl radicals (•OH), beyond the Type-II PDT with the generation of short-lived singlet oxygen ($^1O_2$).[10–15] The ROS-specific generation in cancer cells further results in cellular immunogenic cell death (ICD), priming the cancer immunotherapy and reducing the side effects of phototherapy.[16,17] Type-I PDT is O_2 less dependent, especially due to the O_2 compensation in hypoxic cancer cells by $O_2^{\bullet-}$, which undergoes Haber–Weiss reactions or intratumoral disproportionation.[18,19] By taking account of specific TME, the activable Type-I PDT agent guided by "turn on" imaging modalities is highly required to achieve precision phototheranostics.[20–25]

J. Zhang, H. Luo, W. Ma, J. Lv, B. Wang, F. Sun, Z. Yang
Strait Laboratory of Flexible Electronics (SLoFE)
Fujian Key Laboratory of Flexible Electronics
Strait Institute of Flexible Electronics (Future Technologies)
Fujian Normal University
Fuzhou 350117, China
E-mail: ifezhyang@fjnu.edu.cn

The ORCID identification number(s) for the author(s) of this article can be found under https://doi.org/10.1002/advs.202500293

DOI: 10.1002/advs.202500293

Z. Fang
Department of Oncology and Vascuar Interventonal Therapy
Clinical Oncology School of Fujian Medical University
Fujian Cancer Hospital
Fuzhou 350014, China
E-mail: ztfang@fjzlhospital.com

Z. Fang
Department of imterventional Radiology
shengli Clinical Medical College of Fujian Medical University
Fuijian Provincial Hospital
Fuzhou University Affliated Provincial Hospital
Fuzhou 350001, China

W. Chi
School of Chemistry and Chemical Engineering
Hainan University
Haikou 570228, China
E-mail: weijie_chi@hainanu.edu.cn

Semiconducting open-shell radicals (SORs) owning π-conjugated skeleton, unpaired electrons in their singly occupied molecular orbital (SOMO), narrow optical band gaps, and biocompatibility show strong intermolecular stacking, long-wavelength absorption/emission, and high photothermal conversion, which have potential for cancer phototheranostics.[26–32] Recently, semiconducting closed-shell materials (SCMs) including tetrathiafulvalene, perylene/naphthalene diimide, bipyridine, and π-extended nickel corrole have been modified into their SORs as photothermal agents showing potential for cancer phototheranostics.[33–38] The majority of the SORs are synthesized by their original SCMs receiving electrons from strong reductants and sacrificial electron donors.[39,40] The resulting SORs are usually short-lived and readily return to their SCMs when exposed to air or a physiological environment.[41,42] The SORs also tend to favor non-radiative energy release leading to weak fluorescence emission and almost no photodynamic properties, which greatly hinders their further bioapplications of photo theranostics.[43–45]

To improve the photophysical properties of the SORs to meet the needs of advanced phototheranostics, especially the PDT and fluorescence imaging (FLI) in the second near-infrared region (NIR-II, 1000–1700 nm), we investigate a series of semiconducting perylene diimide (PDI) based SORs with various bromo (Br)-substituents $[PDI(Br)_n]^{\bullet-}$ on the PDI bay/ortho positions (**Figure 1**). According to theoretical calculations, the dihedral angle of aggregated $[PDI(Br)_n]^{\bullet-}$ is enlarged from 0° to 38°, increasing the even number of Br atoms from 0 to 6. Thus, we hypothesize that the introduction of Br groups enhances the PDT and FL properties of $[PDI(Br)_n]^{\bullet-}$, due to the increased heavy atoms effect and weakened π–π stacking energy (from 0.95 to 0.35 eV). Additionally, owing to the electron-drawing effect of Br atoms, the reduction potential of $PDI(Br)_n$ decreases gradually from −402 to −203 mV, and its orbital energy level shifts from −3.99 to −4.41 eV. The $[PDI(Br)_n]^{\bullet-}$ tends to be more stable and more easily obtained in the reducing TME with the increase of Br-substituents. Thus, in this work, the SCMs ($PDI(Br)_6$) with six Br-substituents on the PDI core have been demonstrated easy to get electrons from reducing solutions with mimicking of TME to form SORs ($[PDI(Br)_6]^{\bullet-}$), which is quite stable in the air. After encapsulation by amphiphilic polymer F-127, $PDI(Br)_6$ based nanoparticles ($PDI(Br)_6$ NPs) specifically transform into radical anion $[PDI(Br)_6]$ $NPs^{\bullet-}$ in tumor cells or solid tumors (**Scheme 1**). Due to the rising 808 nm absorbance and NIR-II emission (peak at 1115 nm), $[PDI(Br)_6]$ $NPs^{\bullet-}$ enable the tumor-specific "turn on" photoacoustic imaging (PAI) and NIR-II FLI. Intriguing, the $[PDI(Br)_6]$ $NPs^{\bullet-}$ exhibit a fast electron transfer rate (192.4 ps), which contributes to their catalytic performance for tumor chemodynamic therapy (CDT) by turning O_2 and H_2O_2 into $O_2^{\bullet-}$ and •OH, respectively.[46,47] Furthermore, $[PDI(Br)_6]$ $NPs^{\bullet-}$ show Type-I PDT property of enhanced ROS generation upon 808 laser irradiation. Thus, the $PDI(Br)_6$ NPs achieve tumor-targeted phototherapeutic with minimized side effects and high phototherapeutic efficacy for inhibiting tumor growth. The investigation of activatable PDI-based SORs paves a new avenue of cancer phototheranostics in clinical applications.

2. Results

2.1. Molecular Design, Synthesis and Characterization

Based on the PDI scaffold, four PDI derivatives $PDI(Br)_{0/2/4/6}$ modified with various numbers of Br atoms were synthesized through bromination reaction (Schemes S1–S4, Supporting Information).[48,49] The structures of the intermediates and the target molecules were fully characterized by nuclear magnetic resonance spectroscopy and high-resolution mass spectrometry (HRMS) (Figures S1–S15, Supporting Information). To obtain biocompatible agents, the hydrophobic $PDI(Br)_{0/2/4/6}$ were encapsulated into water-soluble NPs with nanoprecipitation method by using amphiphilic polymer Pluronic F-127 as the surfactant. Dynamic light scattering (DLS) and transmission electron microscopy (TEM) analyses confirmed that $PDI(Br)_6$ NPs exhibited a uniformly spherical morphology with an average hydrodynamic diameter of 104 nm, consistent with that of $PDI(Br)_{0/2/4}$ NPs. The four molecules $PDI(Br)_{0/2/4/6}$ showed a positive charge in solution, and after encapsulation, $PDI(Br)_{0/2/4/6}$ NPs showed negative zeta potential, which demonstrated that the four kinds of PDI were well encapsulated by PF-127 (**Figure 2a**; Figures S16,S17, Supporting Information). The fabrication of nanoparticles allowed PDIs to passively aggregate at tumor sites through enhanced permeability and retention effects. The diameter changes of these NPs were negligible during 14 days' storage in PBS solution supplemented with 10% fetal bovine serum, indicating excellent stability (Figure S18, Supporting Information).

Subsequently, the photophysical properties of four kinds of PDI NPs were investigated by measuring their absorption and fluorescence spectra. The absorption maximum peaks of the $PDI(Br)_{0/2/4/6}$ NPs between 500–600 nm, and the maximum emission peaks were between 550–650 nm (Figures S19,S20, Supporting Information), indicating that the NPs were difficult to carry out NIR-II imaging and therapy in vivo.[50,51] We then investigated the potential of PDI SORs by reduction of $PDI(Br)_{0/2/4/6}$ for cancer theranostics.[52] In this work, strong reducing agent sodium dithionate ($Na_2S_2O_4$) and weak reducing agent sodium thiosulfate ($Na_2S_2O_3$) were utilized as to explore the generation of PDI SORs.[53] After reacting with $Na_2S_2O_4$, the absorption of the four kinds of PDI NPs all displayed new peaks at 600–1100 nm, indicating the formation of PDI SORs. However, when $Na_2S_2O_3$ solution was introduced, only $PDI(Br)_4$ NPs and $PDI(Br)_6$ NPs were reduced to the corresponding SORs showing the maximum absorption peak at 765 and 798 nm, respectively (Figure 2b; Figures S21,S22, Supporting Information). Additionally, the first reduction peak of $PDI(Br)_0$, $PDI(Br)_2$, $PDI(Br)_4$, and $PDI(Br)_6$ were observed at −402, −347, −289, and −203 mV versus Ag/AgCl in solutions, respectively (Figure S23, Supporting Information). The lowest unoccupied molecular orbitals (LUMOs) and the highest occupied molecular orbitals (HOMOs) of these compounds were primarily distributed along the PDI molecular backbone. Meanwhile, the theoretical calculations estimated LUMO values of −3.99, −4.16, −4.3, and −4.41 eV for the four PDIs, respectively (Figure 2d; Figures S24,S25, Supporting Information), demonstrating that $PDI(Br)_4$ NPs and $PDI(Br)_6$

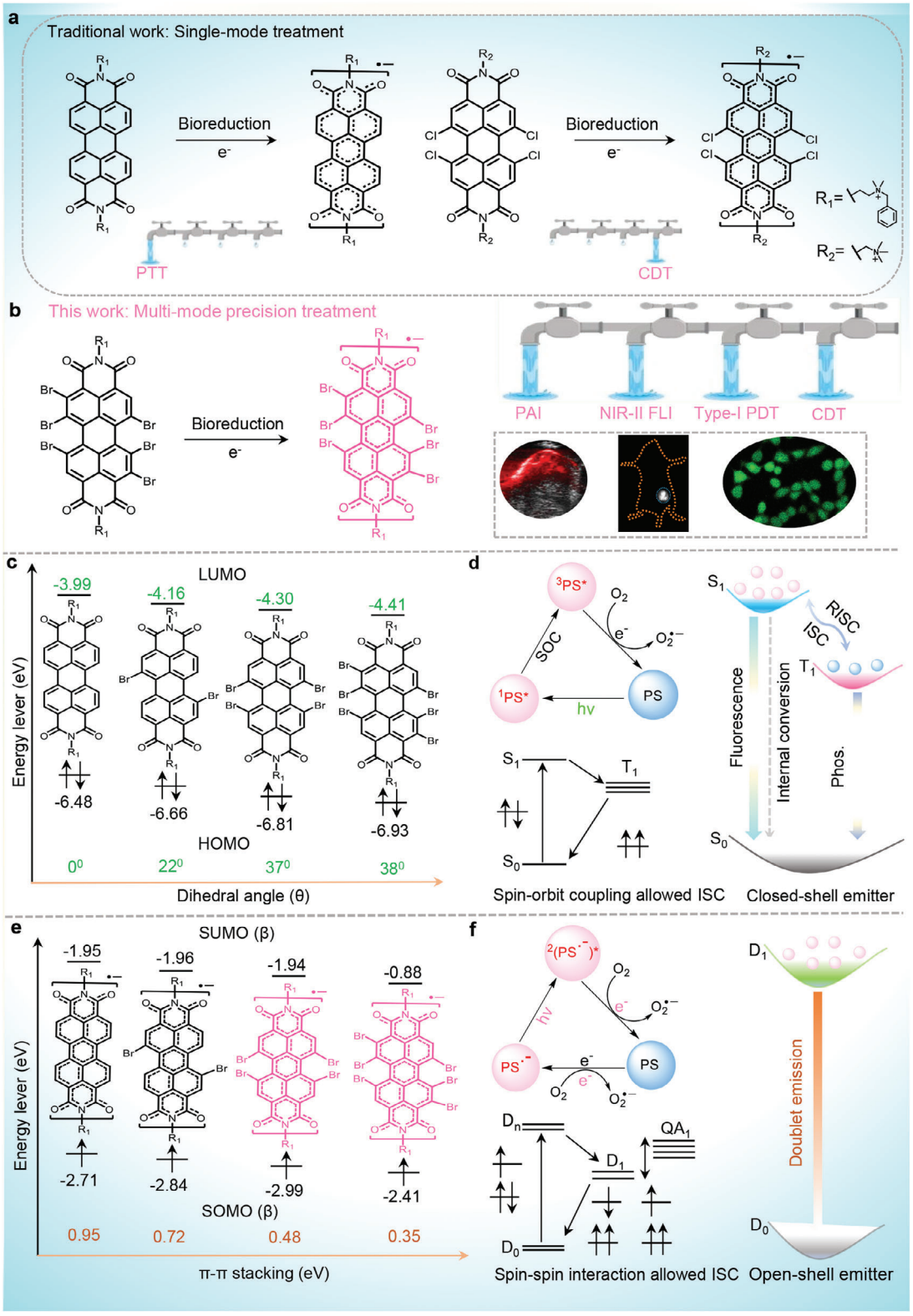

Figure 1. Traditional single-mode treatment, multi-mode precision treatment, and photophysical processes involved in Type-I PDT and luminescence for PDI semiconducting closed-shell and open-shell radicals. a) The single-model treatment (traditional strategies)[46,47,60] and b) multi-mode precision treatment for cancer of PDI semiconducting open-shell radicals (this work). c,d) The chemical structures, energy levels, dihedral angle, spin–orbit coupling allowed ISC and luminescence mechanism of PDI closed-shell materials.[64–66] e,f) The chemical structures, energy levels, π–π stacking energy levels, spin–spin interaction allowed ISC and luminescence mechanism of PDI open-shell radicals.[39,67–69]

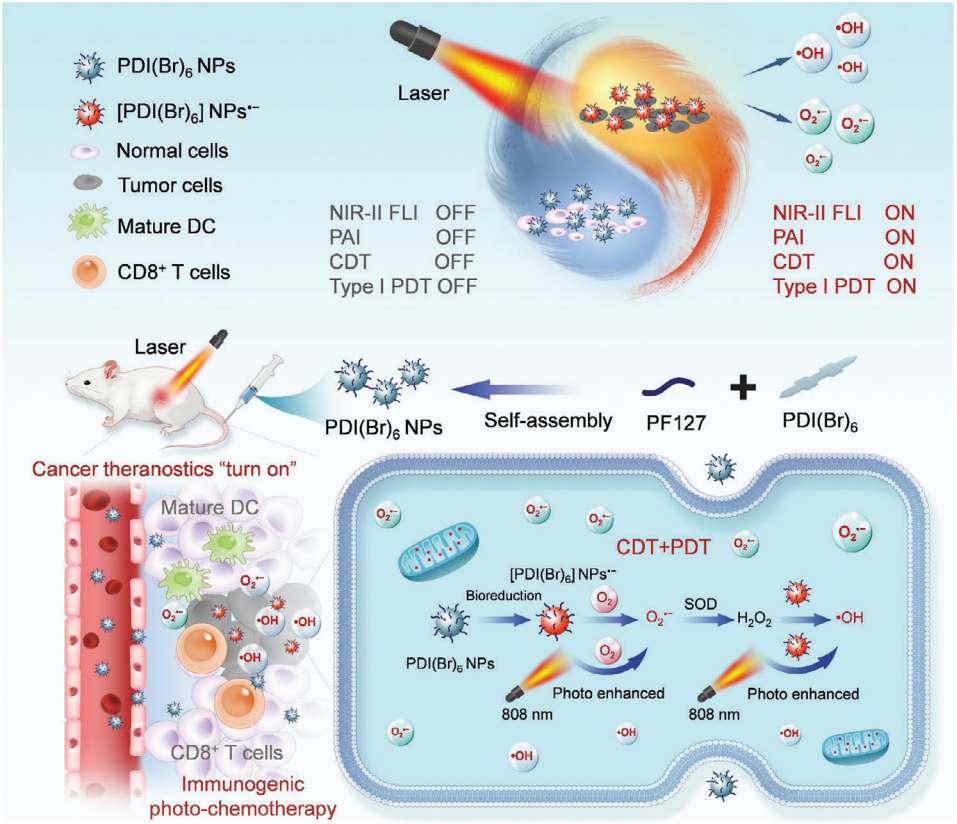

Scheme 1. Schematic of a cancer theranostic nanoplatform of activatable PDI semiconducting open-shell radicals (PDI SORs) for combined chemodynamic/photodynamic therapy (CDT/PDT) guided by NIR-II fluorescence imaging (FLI) and PA imaging (PAI).

NPs were more easily to transform into the SORs $[PDI(Br)_4]$ $NPs^{\bullet-}$ and $[PDI(Br)_6]$ $NPs^{\bullet-}$ under mild reduction environment, such as TME.

We then investigated the above NIR-II fluorescence emission of the four kinds of PDI NPs after the reaction with $Na_2S_2O_4$ and $Na_2S_2O_3$ by using 808 nm laser irradiation. After reaction with $Na_2S_2O_4$, $PDI(Br)_0$ NPs showed barely NIR-II emission, the other three kinds of PDI NPs exhibited strong NIR-II emission in the range of 900–1400 nm. However, under reaction with $Na_2S_2O_3$, $PDI(Br)_0$ NPs and $PDI(Br)_2$ NPs both showed no NIR-II fluorescence emission, and $PDI(Br)_4$ NPs and $PDI(Br)_6$ maintained intensive NIR-II fluorescence emission (Figure 2c; Figures S26,S27, Supporting Information). The absence of NIR-II fluorescence emission was likely attributed to the tendency π–π stacking of $PDI(Br)_0$ nanoparticles in water, leading to the fluorescence quenching of SORs. Subsequently, we tested the stability performance of the generated PDI SOCs. $[PDI(Br)_4]$ $NPs^{\bullet-}$ and $[PDI(Br)_6]$ $NPs^{\bullet-}$ produced from $Na_2S_2O_3$, exhibited prolonged photophysical stability under hypoxic conditions and across various environments, including different pH levels, serum solutions, and photothermal stability (Figure 2e,f; Figures S28–S33, Supporting Information).

To further explore the mechanism of the bright NIR-II fluorescence emission and excellent stability of $[PDI(Br)_4]$ $NPs^{\bullet-}$ and $[PDI(Br)_6]$ $NPs^{\bullet-}$, various molecular properties, including the dihedral angle, interaction mode, electron delocalization index (EDI) and singly unoccupied molecular orbital of the four $PDI(Br)_{0/2/4/6}$ were analyzed at the U-B3LYP/Def2SVP level. The dihedral angle between the $[PDI]^{\bullet-}$ was calculated to be 38°, 37°, 22°, and 0° for $[PDI(Br)_6]^{\bullet-}$, $[PDI(Br)_4]^{\bullet-}$, $[PDI(Br)_2]^{\bullet-}$ and [PDI(Br)0]•−, respectively (Figure 2g; Figures S34,S35, Supporting Information). These results indicate that the introduction of bromine (Br) atoms restricts π–π stacking between [PDIs]•− molecules, thereby enhancing the stability of the PDI SORs. To further analyze the superiorities of twisted molecule strategy, quantum chemical molecular dynamics simulations were performed on four $[PDIs]^{\bullet-}$. Clearly, $[PDI(Br)_4]^{\bullet-}$ and $[PDI(Br)_6]^{\bullet-}$ consistently maintained a twisted conformation, whether in a single-molecule state or aggregate state. The π–π stacking energy of the four $[PDI(Br)_{0/2/4/6}]^{\bullet-}$ decreased gradually from 0.95 to 0.35 eV (Figure 2h). These findings supported the importance of the twisted molecular structure in stabilizing SORs and facilitating NIR-II fluorescence emission. A decrease in both EDI and the energy of the SOMOs on the α and β orbitals was observed, with values ranging from 4.74 to 4.53 and −2.71/−2.71 to −1.45/−2.41 eV, respectively (Figure 2i,j; Figure S36, Supporting Information), indicating reduced reactivity at a single atom and overall enhanced stability of the molecule due to spin delocalization within the large π-system.[54]

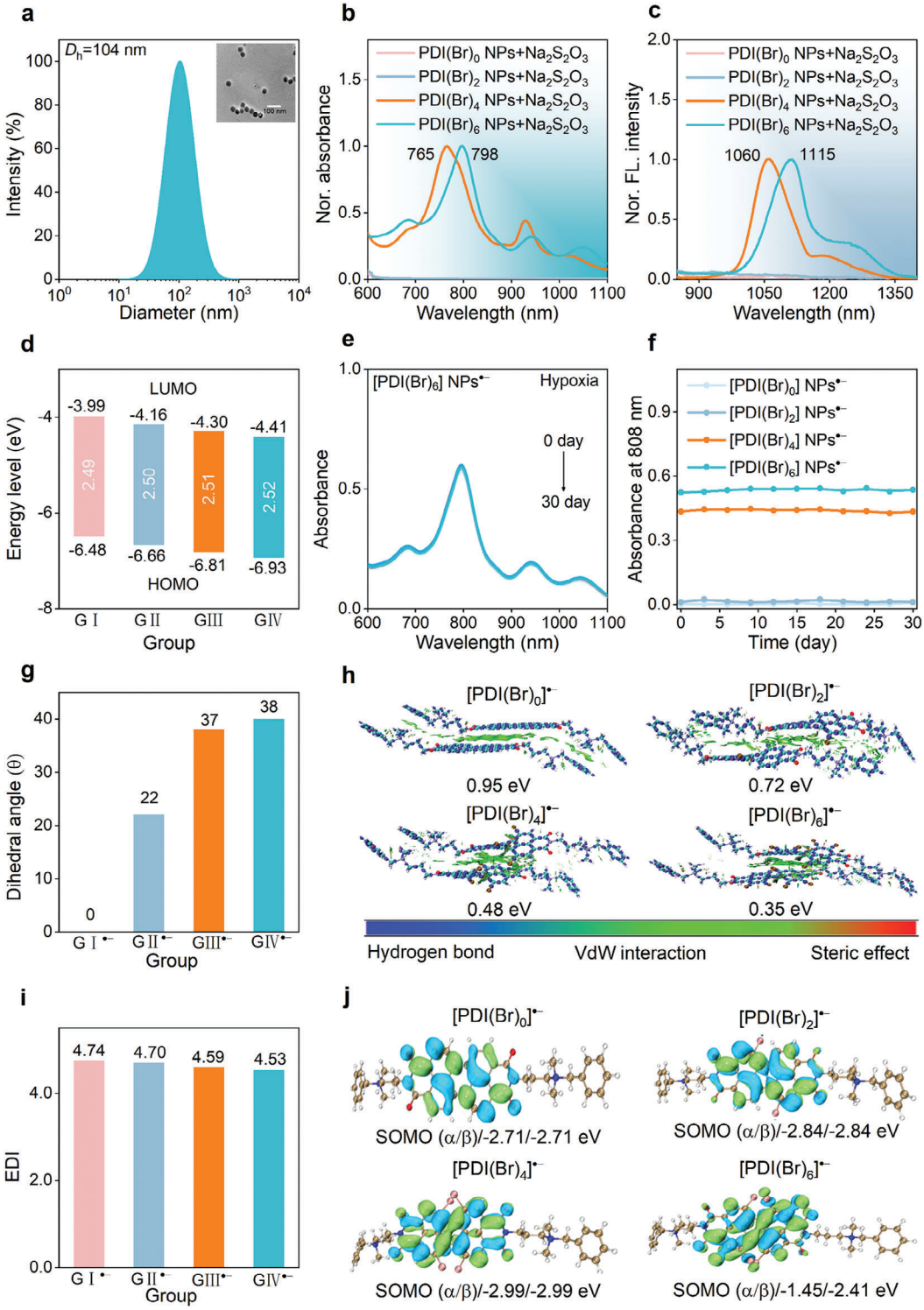

Figure 2. Photophysical properties studies of the molecular PDI(Br)$_n$ and nanoparticle PDI(Br)$_n$ NPs and their corresponding radicals. a) DLS analysis of PDI(Br)$_6$ NPs. Inset: TEM image of PDI(Br)$_6$ NPs. b) Normalized absorption and c) NIR-II fluorescence spectra of PDI(Br)$_n$ NPs (0.2 mM, 2.5 mL) obtained by titration with $Na_2S_2O_3$ solution. d) The calculated HOMO, LUMO, and energy levels of the four kinds of PDI(Br)$_{0/2/4/6}$. e) After reaction with $Na_2S_2O_3$, time-dependent absorption spectra of [PDI(Br)$_6$] NPs$^{•-}$ and f) comparison of the absorption stability of four radials [PDI(Br)$_n$] NPs$^{•-}$ recording at 808 nm during 30 days in PBS under hypoxia conditions. g) The calculated dihedral angle distribution and h) simulated interaction modes and interaction energies of the four kinds of [PDI(Br)$_n$]$^{•-}$ in their aggregates, respectively. i) The calculated electron delocalization index levels and j) molecular orbital energy levels of the four kinds of [PDI(Br)$_n$]$^{•-}$. GI/GI$^{•-}$: PDI(Br)$_0$/[PDI(Br)$_0$]$^{•-}$, GII/GII$^{•-}$: PDI(Br)$_2$/[PDI(Br)$_2$]$^{•-}$, GIII/GIII$^{•-}$: PDI(Br)$_4$/[PDI(Br)$_4$]$^{•-}$, GIV/GIV$^{•-}$: PDI(Br)$_6$/[PDI(Br)$_6$]$^{•-}$.

2.2. Chemo/Photodynamic Properties of PDI SORs

Encouraged by the remarkable stability and optical properties of [PDI(Br)$_{4/6}$] NPs$^{\bullet-}$, we further investigated their photodynamic and chemodynamic electron transfer performance for the generation of ROS, such as $O_2^{\bullet-}$ and •OH, by using an 808 nm laser (Figure S37, Supporting Information).[47] The overall ROS generation capabilities were evaluated using ROS-sensitive dichlorodihydrofluorescein (DCFH) as a generation indicator. The fluorescence at 525 nm showed a slow increase in the presence of [PDI(Br)$_4$] NPs$^{\bullet-}$ and [PDI(Br)$_6$] NPs$^{\bullet-}$, respectively. However, a significant fluorescence increase was observed upon 808 nm (0.3 W cm^{-2}) laser irradiation upon above the solutions (Figures S38–S40, Supporting Information). The comparison of the ROS-producing capacity of the experimental groups was PBS < [PDI(Br)$_4$] NPs$^{\bullet-}$ < [PDI(Br)$_6$] NPs$^{\bullet-}$ < [PDI(Br)$_4$] NPs$^{\bullet-}$ + laser < [PDI(Br)$_6$] NPs$^{\bullet-}$ + laser. To distinguish the specific ROS species in the system, we utilized dihydrorhodamine 123 (DHR123) to detect the generation of $O_2^{\bullet-}$. In the absence of laser irradiation, both [PDI(Br)$_6$] NPs$^{\bullet-}$ and [PDI(Br)$_4$] NPs$^{\bullet-}$ exhibited a slight fluorescence intensity of DHR123 compared to the PBS group. Surprisingly, upon near-infrared (NIR) light irradiation, the fluorescence intensity of DHR123 in both solutions was significantly enhanced. The results indicated that both [PDI(Br)$_6$] NPs$^{\bullet-}$ and [PDI(Br)$_4$] NPs$^{\bullet-}$ showed CDT and Type-I PDT abilities (**Figure 3a**; Figures S41–S43, Supporting Information). To accurately determine the production of $O_2^{\bullet-}$, ESR spectroscopy was performed using 5-tert-butoxycarbonyl-5-methyl-1-pyrroline N-oxide (BMPO) as a spin-trapping reagent. Without laser irradiation, slight $O_2^{\bullet-}$ signals were detected by the ESR in solutions of [PDI(Br)$_6$] NPs$^{\bullet-}$ and [PDI(Br)$_4$] NPs$^{\bullet-}$. Moreover, enhanced ESR signals were observed upon laser irradiation in above the solutions (Figure 3b). To further investigate whether [PDI(Br)$_6$] NPs$^{\bullet-}$ and [PDI(Br)$_4$] NPs$^{\bullet-}$ produced •OH in the H_2O_2 solution, •OH-specific probes hydroxyphenyl fluorescein (HPF) were employed in experiments. The [PDI(Br)$_6$] NPs$^{\bullet-}$ and [PDI(Br)$_4$] NPs$^{\bullet-}$ exhibited moderate •OH generation abilities without laser. Under laser irradiation, the production amount of •OH was improved. Notably, [PDI(Br)$_6$] NPs$^{\bullet-}$ substantially increased the fluorescence intensity of HPF by 7.81-fold compared to PBS and 1.67-fold compared to [PDI(Br)$_4$] NPs$^{\bullet-}$ (Figure 3c; Figures S44,S45, Supporting Information). The generation of •OH was also confirmed by ESR analysis (Figure 3d), using DMPO as spin trapping agents. Without laser irradiation, the slight •OH signals were detected in the ESR spectrum for [PDI(Br)$_4$] NPs$^{\bullet-}$ and [PDI(Br)$_6$] NPs$^{\bullet-}$. In contrast, enhanced ESR signals were observed upon laser irradiation. Singlet oxygen ($^1O_2$) signals of the two radicals were almost silent under the same experimental conditions (Figure S46, Supporting Information). All in all, both [PDI(Br)$_6$] NPs$^{\bullet-}$ and [PDI(Br)$_4$] NPs$^{\bullet-}$ could boost •OH and $O_2^{\bullet-}$ production, which beneficial for cancer CDT/PDT combination therapy.

To comprehensively understand the ROS-generation mechanism of the SORs, theoretical calculations were performed by capitalizing on time-dependent density functional theory. The electron density diagrams illustrated an increase in electron density from PDI to PDI$^{\bullet-}$ (Figure 3e,f; Figures S47,S48, Supporting Information). The electron distribution on the surface of PDI$^{\bullet-}$ was notably high, facilitating the direct sensitization of oxygen O_2 to produce $O_2^{\bullet-}$. Upon light irradiation, PDI$^{\bullet-}$ was excited to the doublet excited state, ^{2}(PDI$^{\bullet-}$)*, which enhanced electron transfer to O_2, resulting in significant $O_2^{\bullet-}$ generation.[55,56] Due to the immaturity of intersystem crossing (ISC) process calculation on SORs, thus we investigated the ISC process of PDI SCMs as lateral evidence to demonstrate the enhancement of photoelectronic process with an increase of Br atoms on the PDI skeleton. With Br substituents from 0 to 6, PDIs showed a decreased energy gap ΔE_{ST} from 1.434 to 1.307 eV. The spin–orbit coupling constants ξ of PDI(Br)$_6$ even reached S_1, T_1 = 1.89 cm^{-1}, S_1, T_2 = 34.28 cm^{-1}, showing a highly enhanced ISC pathway for promoting photoelectronic transfer (Figure 3g). Strengthening the above-proposed mechanism, the fs-TA spectroscopy of [PDI(Br)$_4$] $^{\bullet-}$ and [PDI(Br)$_6$]$^{\bullet-}$ were obtained by exciting at its peak absorption (750 nm). The positive absorption from 600 and 750 nm corresponds to the excited state absorption of ^{2}(PDIs$^{\bullet-}$)*, and the negative absorption at 900–1000 nm corresponds to the ground state bleach (GSB) of PDI$^{\bullet-}$ (Figure 3h,j).[56,57] We quantitatively analyzed the GSB rates of [PDI(Br)$_4$]$^{\bullet-}$ and [PDI(Br)$_6$]$^{\bullet-}$. The results showed that the average lifetime of [PDI(Br)$_6$]$^{\bullet-}$ (192.4 ps) is shorter than that of [PDI(Br)$_4$] $^{\bullet-}$ (319.4 ps), further indicated that [PDI(Br)$_6$]$^{\bullet-}$ had more efficient electron transfer (Figure S49, Supporting Information).[58] Results also were revealed from the 2D pseudocolor fs-TA spectra that the GSB signal of [PDI(Br)$_6$]$^{\bullet-}$ exhibited relatively fast attenuation (Figure 3i,k).[59] Overall, the rapid electron transfer process within the [PDI(Br)$_6$]$^{\bullet-}$ under laser exposure further amplified ROS production efficiency, particularly favoring the Type-I PDT pathway.

Hypoxic tumors generally exhibit strong reducibility due to the high accumulation of reducing substances such as reducing complexes (GSH), reducing enzymes (GSH reductase), reducing amino acids (cysteine), and nicotinamide adenine dinucleotide phosphate NAD(P)H.[60,61] To investigate the conversion of PDI NPs into PDI NPs$^{\bullet-}$ in hypoxic tumor cells, ESR spectroscopy and NIR-II fluorescent images were conducted. As shown in Figure 3l,m and Figure S50 (Supporting Information), the ESR and NIR-II fluorescence signals were observed in the presence of various tumor cells under hypoxic conditions, suggesting the formation of [PDI(Br)$_6$] NPs$^{\bullet-}$. In contrast, there were no ESR and fluorescence signals in the presence of normal cells under normoxic conditions. We then compared the ESR signals of the four PDI(Br)$_{0/2/4/6}$ NPs after incubation with 4T1 tumor cells, indicating that increased ESR signals by the increase of the Br atoms on the PDI skeleton (Figure 3n). Although the PDI(Br)$_{0/2}$ NPs showed ESR signals with 4T1 tumor cells, the signals were quenched in the 7 days of exposure in the air, but the signals of PDI(Br)$_{4/6}$ NPs were enduring in the same condition (Figure S51, Supporting Information). Further, the spin density calculations of the four kinds of PDI SORs revealed that the single electron were delocalized across the whole PDI skeleton. Specifically, incorporating of Br atoms into the PDI enhanced electron delocalization within the intramolecular bonds of SORs, which was beneficial to reducing the reactivity on a single atom, improving the molecule's overall stability (Figures S52,S53, Supporting Information). In conclusion, the excellent photostability, ROS generation ability, and hypoxic tumor-specific activation of PDI(Br)$_6$ NPs allowed to further biomedical applications.

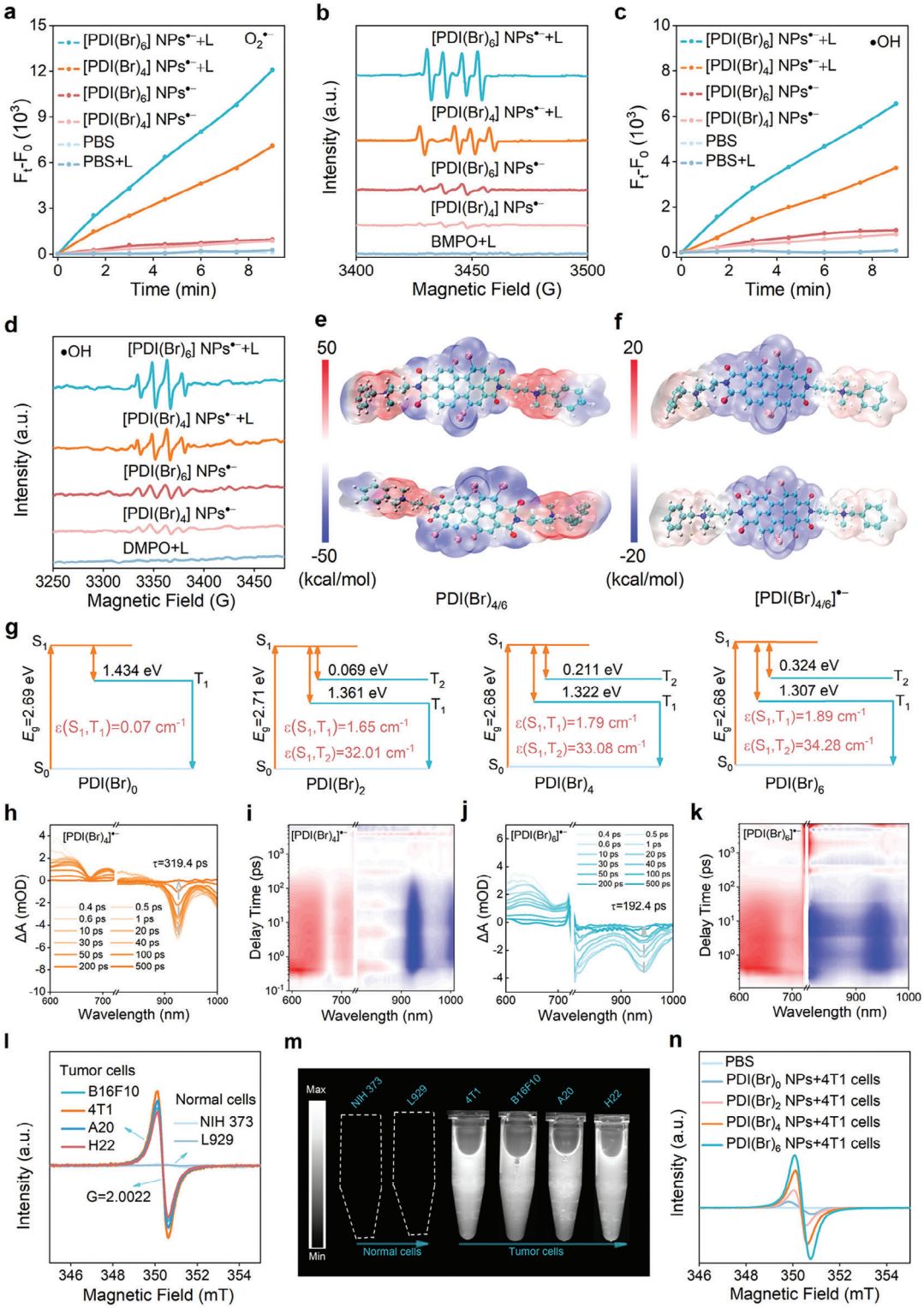

Figure 3. ROS performance, electrostatic potential (ESP), ultrafast femtosecond transient absorption (fs-TA), and electron spin resonance (ESR) spectra of $[PDI(Br)_n]$ $NPs^{\bullet-}$. a) Comparison of the $O_2^{\bullet-}$ generation capacity of $[PDI(Br)_4]$ $NPs^{\bullet-}$ and $[PDI(Br)_6]$ $NPs^{\bullet-}$ with or without laser irradiation (0.3 W cm^{-2} at 808 nm). b) ESR signals of BMPO for $O_2^{\bullet-}$ characterization in the presence of $[PDI(Br)_4]$ $NPs^{\bullet-}$ and $[PDI(Br)_6]$ $NPs^{\bullet-}$ containing BMPO (DMSO: H_2O = 1: 9, v/v) before and after 808 nm laser for 10 min. [BMPO] = 0.15 M. c) Comparison of the •OH generation capacity of $[PDI(Br)_4]$ $NPs^{\bullet-}$ and $[PDI(Br)_6]$ $NPs^{\bullet-}$ with or without laser irradiation (0.3 W cm^{-2} at 808 nm). H_2O_2 (0.2 mM) was added to all test solutions. d) ESR signals of DMPO for •OH characterization in the presence of $[PDI(Br)_4]$ $NPs^{\bullet-}$ and $[PDI(Br)_6]$ $NPs^{\bullet-}$ containing DMPO (DMSO: H_2O = 1: 9, v/v) before and after 808 nm laser for 10 min. [DMPO] = 0.15 M. H_2O_2 (0.2 mM) was added to all the test solutions to obtain •OH. e) Electrostatic potential (ESP) distributions of

2.3. ROS Performance of PDI(Br)$_6$ NPs on the Cellular Level

Based on the CDT/PDT performance, we first investigated the cytotoxicity of PDI(Br)$_6$ NPs on L929 cells and 4T1 cancer cells by cell counting kit-8 (CCK-8) assays. Results demonstrated that PDI(Br)$_6$ NPs showed negligible cytotoxicity with or without 808 nm laser irradiation on L929 cells, indicating it had good biocompatibility on normal cells. However, obvious 4T1 cell death was observed with the treatment of PDI(Br)$_6$ NPs with or without 808 nm laser (**Figure** 4a,b). The half-maximal inhibitory concentration (IC50) of PDI(Br)$_6$ NPs was less than 10 μM under laser in the hypoxic environment, indicating that PDI(Br)$_6$ NPs were specifically activated in hypoxic tumor cells with excellent CDT and Type-I PDT properties. DCFH-DA was used to evaluate the intracellular ROS-producing capability of PDI(Br)$_6$ NPs by confocal laser scanning microscopy and flow cytometry. When 4T1 cells were treated exclusively with PDI(Br)$_6$ NPs, green signals associated with ROS were observed, suggesting that the PDI(Br)$_6$ NPs were activated into [PDI(Br)$_6$] NPs$^{\bullet-}$ and then induced endogenous ROS generation under hypoxic conditions. After laser irradiation, strong green fluorescence signals were observed, revealing the PDT of [PDI(Br)$_6$] NPs$^{\bullet-}$ in 4T1 cells performed (Figure 4d, Top). The same results were obtained by flow cytometry (Figure S54, Supporting Information). Subsequently, intracellular $O_2^{\bullet-}$ generation was detected by dihydroethidium (DHE) fluorescent probe. Red fluorescence signals were observed in the PDI(Br)$_6$ NPs-treated 4T1 cells under hypoxic conditions, and the signals became brighter after laser irradiation (Figure 4d, Bottom), indicating the $O_2^{\bullet-}$ is the main component of the generated endogenous ROS. As known, $O_2^{\bullet-}$ can trigger a series of reactions to the production of H_2O_2 and O_2.[47,62,63] Additionally, [PDI(Br)$_6$] NPs$^{\bullet-}$ reacted with H_2O_2 to produce •OH. Thus, we used commercial H_2O_2 and •OH probes to quantify their endogenous generation, respectively. The results indicated that [PDI(Br)$_6$] NPs$^{\bullet-}$ increased the fluorescence of cells by 1.86-fold for H_2O_2 and 1.67-fold for •OH compared to the PBS group. Predictably, when exposed the treated cells to an 808 nm laser, the significantly enhanced fluorescence by 3.24-fold for H_2O_2 and 4.75-fold for •OH compared to the PBS group. All the results provided strong evidence for the CDT and Type-I PDT properties of PDI(Br)$_6$ NPs in tumor cells (Figure 4c; Figures S55,S56, Supporting Information). Furthermore, the therapeutic efficacy of PDI(Br)$_6$ NPs toward 4T1 cells with or without laser was confirmed visually by live/dead cell costaining and flow cytometry examination (Figure 4e; Figure S57, Supporting Information). To confirm the burst release of ROS from the CDT/PDT inducing strong ICD effect, we examined the damage-associated molecular patterns (DAMPs) on the cellular level, including monitoring ATP secretion, CRT expression, and HMGB1 release, after the treatment of PDI(Br)$_6$ NPs with laser irradiation (Figure 4f; Figures S58–S60, Supporting Information). PDI(Br)$_6$ NPs incubation with 4T1 cells with and without laser irradiation showed ATP release with 2.37-fold and 4.46-fold enhancement compared to the PBS group, respectively. The CRT exposure and HMGB1 release in 4T1 cells also showed the same tendency, indicating the PDI(Br)$_6$ NPs with laser irradiation has the potential to release DAMPs for recruitment of antigen-presenting cells and prime antitumor immune response.

2.4. Activable Bioimaging of PDI(Br)$_6$ NPs In Vivo

To determine the optimal time window for photoimmunotherapy, PDI(Br)$_6$ NPs were intravenously injected into 4T1 tumor-bearing mice, and the tumor accumulation and the [PDI(Br)$_6$] NPs$^{\bullet-}$ production were monitored by PAI and NIR-II FLI (**Figure** 5a). We initially explored the tumor-specific activation capability of the PDI NPs in 4T1 tumor-bearing mice through PA imaging under an 808 nm laser. Following the intravenous injection of PDI(Br)$_6$ NPs into the 4T1 tumor-bearing mice, time-dependent PA images were collected (Figure 5b,c). PA intensities gradually increased over time and reached maximum signals at 12 h post-injection, indicating the [PDI(Br)$_6$] NPs accumulated tumor sites and were specifically activated into the corresponding PDI SORs.

We then investigated the activatable NIR-II FLI of the PDI NPs by intravenously injecting of PDI(Br)$_{0/4/6}$ NPs into 4T1 tumor-bearing mice, respectively and time-dependent whole-body NIR-II signals were collected. The NIR-II fluorescence of tumors with PDI(Br)$_4$ NPs and PDI(Br)$_6$ NPs exhibited a gradual increase in tumor, and the signals reached to the peak at 12 h post-injection. At 36 h post-injection, we recorded the ex vivo NIR-II FLI of the mice dissected tumor and major organs (Figure 5d–g; Figures S61,S62, Supporting Information). As proof of concept, we found that only the tumor had been lit by the PDI(Br)$_4$ NPs and PDI(Br)$_6$ NPs, whereas the main organs (heart, liver, spleen, lung, kidneys and intestines) showed barely visible signals. In sharp contrast, after intravenous injection of PDI(Br)$_0$ NPs, no NIR-II fluorescence signal was obtained in 4T1 tumor-bearing mice due to the π–π stacking-induced quenching of fluorescence signal (Figure S63, Supporting Information). To further explore the tumor specificity of PDI(Br)$_{4/6}$ NPs, after intravenous injection of the PDI(Br)$_{4/6}$ NPs into the healthy mice, no NIR-II optical signals were detected in the healthy mice and the main organs (Figures S64,S65, Supporting Information). Conclusively, all the results validated that the PDI(Br)$_{4/6}$ NPs enabled activatable tumor PAI/NIR-II FLI for guiding the chemo/photodynamic combination therapy.

2.5. Chemo/Photodynamic Combination Therapy of PDI(Br)$_6$ NPs

Encouraged by the performance of synergetic therapeutic efficacy, high tumor accumulation, and specific activation of

PDI(Br)$_4$ (top), PDI(Br)$_6$ (bottom), f) [PDI(Br)$_4$]$^{\bullet-}$ (top) and [PDI(Br)$_6$]$^{\bullet-}$ (bottom), respectively. g) The energy level diagrams and SOC coefficients for the four kinds of PDI(Br)$_n$. The femtosecond transient absorption spectra of h,i) [PDI(Br)$_4$]$^{\bullet-}$ and j,k) [PDI(Br)$_6$]$^{\bullet-}$ with a 750 nm photoirradiation at different pump-probe delay times. l) ESR spectra and m) NIR-II FLI of the [PDI(Br)$_6$]$^{\bullet-}$ generated from PDI(Br)$_6$ NPs in the presence of various tumor cells under hypoxic conditions and normal cells under normoxic conditions. n) ESR spectrum of the four kinds of PDI(Br)$_n$ NPs incubating with 4T1 tumor cells.

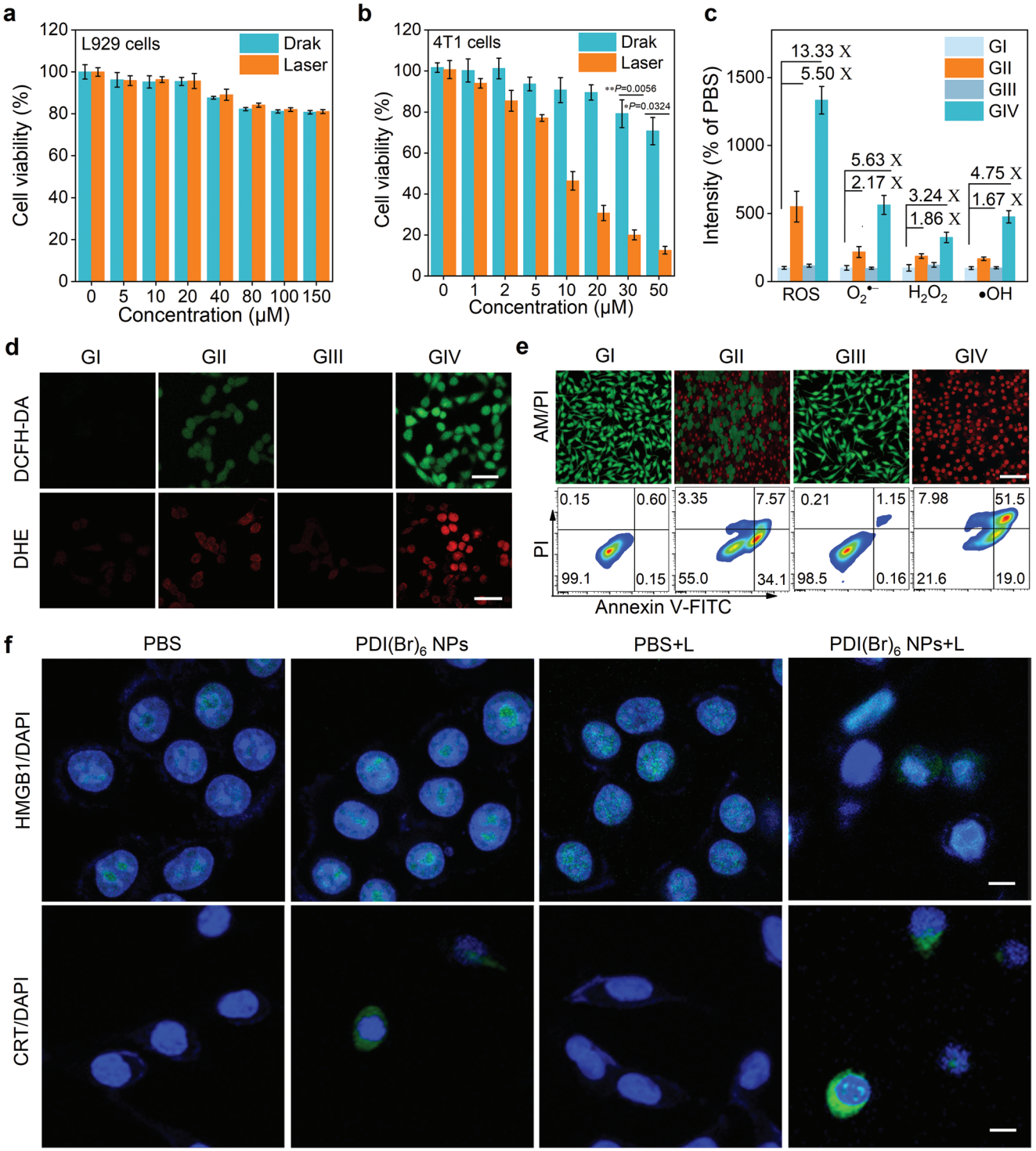

Figure 4. In vitro cellular research on the phototheranostics of $PDI(Br)_6$ NPs. Cell viabilities of a) L929 cells and b) 4T1 cells after treatment of $PDI(Br)_6$ NPs with or without laser irradiation (0.3 W cm^{-2} at 808 nm). Data are presented as mean ± SD (n = 4 independent experiments). c) Quantitative fluorescence analysis of total ROS, $O_2^{\bullet-}$, H_2O_2 and •OH in 4T1 cells after treatment of PBS and $PDI(Br)_6$ NPs for 12 h with or without laser irradiation (0.3 W cm^{-2} at 808 nm). Data are presented as mean ± SD (n = 3 independent experiments). d) Representative imaging of DCFH-DA (ROS), dihydroethidium (DHE) ($O_2^{\bullet-}$) in 4T1 cells treated with PBS or $PDI(Br)_6$ NPs for 12 h with or without laser irradiation (0.3 W cm^{-2} at 808 nm). Scale bars: 50 μm. e) Live/dead cells staining (top) and cell apoptosis assay (bottom) of 4T1 cells after various treatments, Scale bars: 50 μm. f) Representative images of the HMGB1 release (top) and CRT exposure (bottom) on 4T1 cancer cells after various treatments. Scale bars: 40 μm. GI: PBS, GII: $PDI(Br)_6$ NPs, GIII: PBS+laser, GIV: $PDI(Br)_6$ NPs+laser.

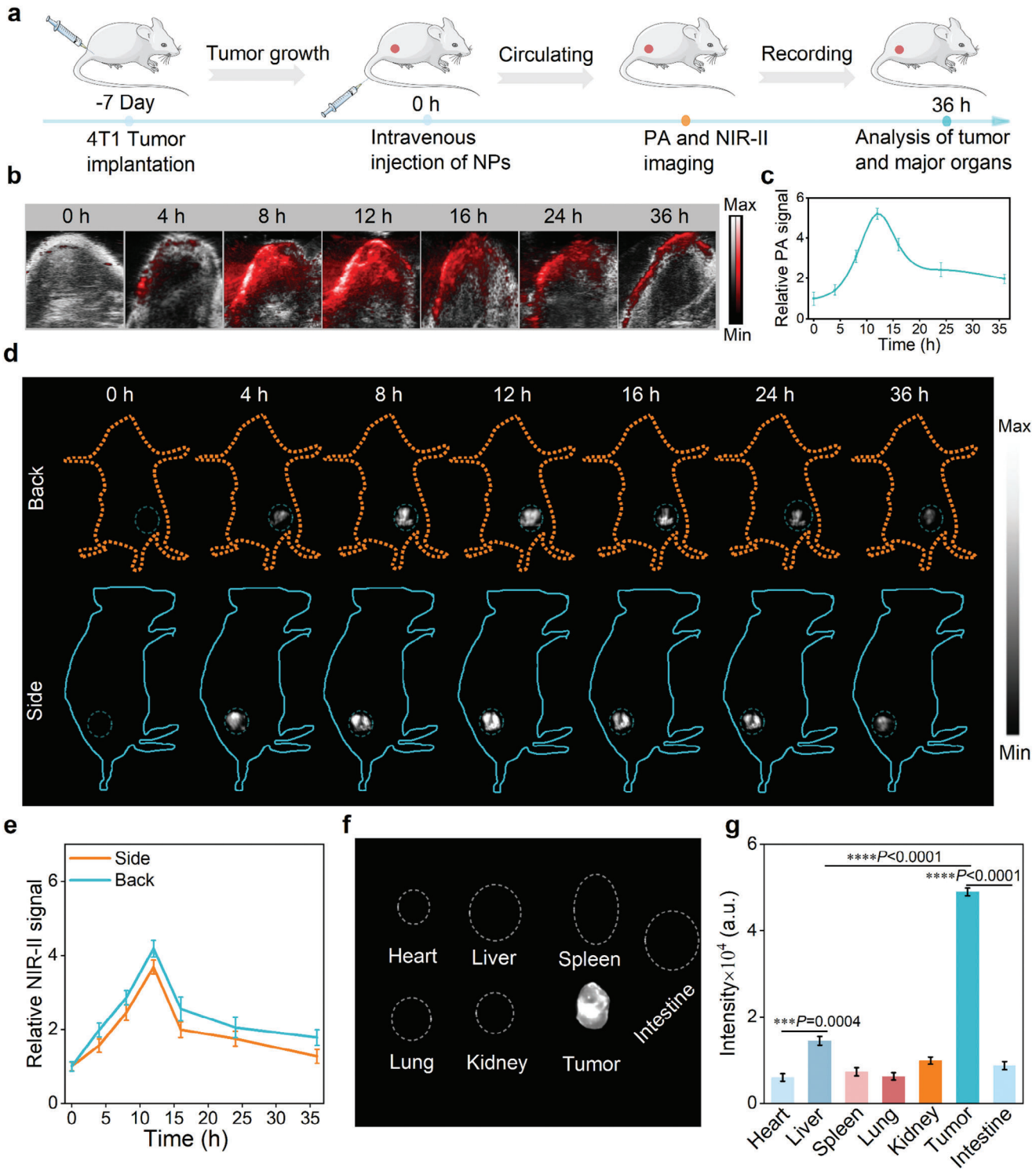

Figure 5. In vivo PAI and NIR-II FLI of $PDI(Br)_6$ NPs on 4T1 bearing mice. a) Experimental outline recording the PAI and NIR-II FLI steps and procedures in 4T1 tumor-bearing mice. Representative tumor-specific b,c) PAI and d,e) NIR-II FLI and their corresponding intensities of 4T1 tumor-bearing mice at different time points after intravenous injection of $PDI(Br)_6$ NPs, respectively. Data are presented as mean ± SD ($n = 3$). f,g) The NIR-II FLI and the corresponding fluorescence intensities of the major organs and tumors from mice after 36 h post-injection of $PDI(Br)_6$ NPs. Data are presented as mean ± SD ($n = 3$).

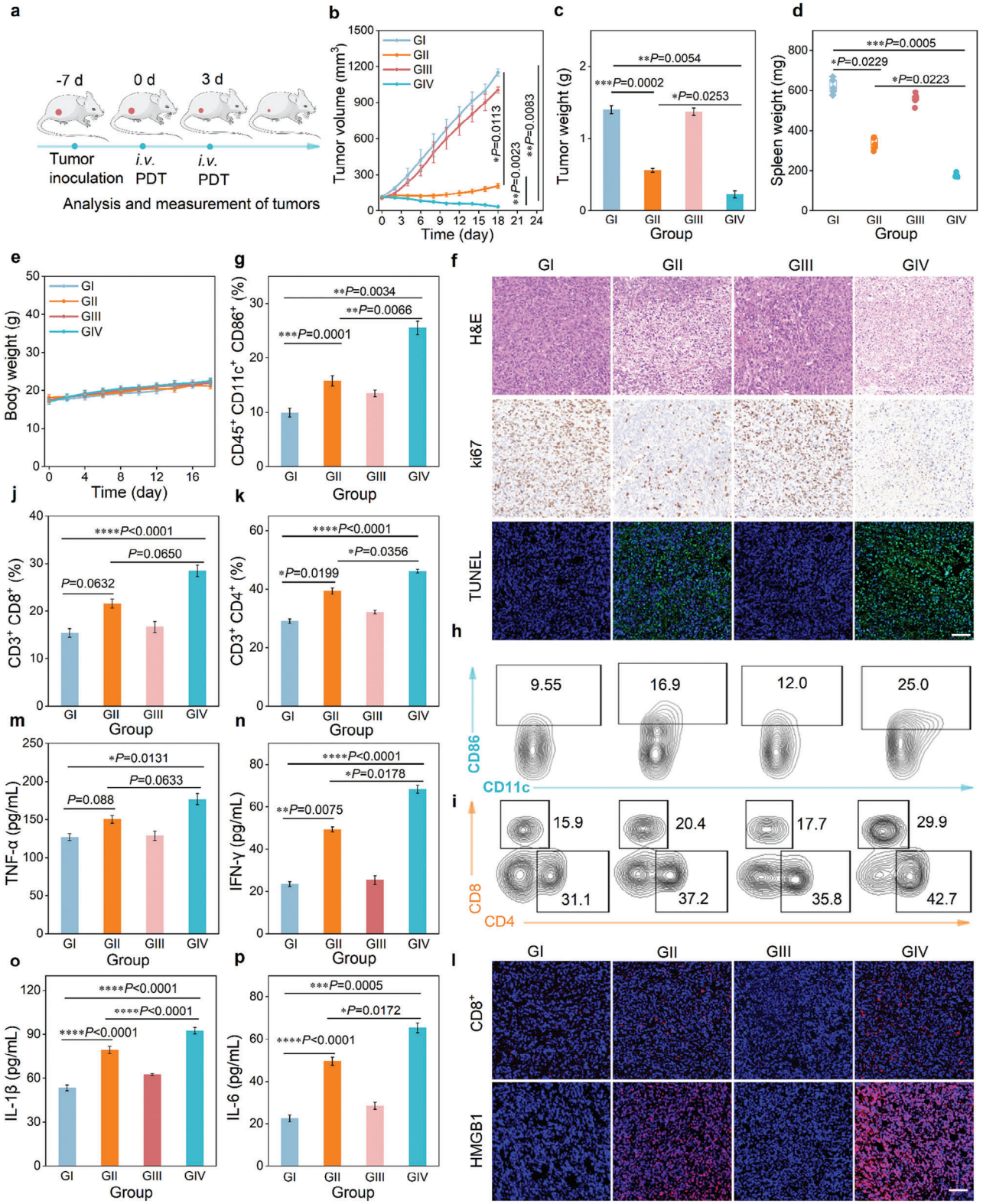

Figure 6. Evaluation of the in vivo therapeutic efficacy of $PDI(Br)_6$ NPs. a) Experimental timeline of the treatments and procedures for evaluating the therapeutic outcomes in 4T1 tumor-bearing mice. b) Tumor volume changes of the mice in each group during the treatment period. c) Tumor weight, d) spleen size, and e) body weight changes of mice in each group during the treatment period. Data are presented as mean ± SD (n = 5 mice). f) Representative H&E, Ki67, TUNEL staining of tumor sections harvested from the mice receiving various treatments. Scale bars: 100 μm. g,h) Representative flow cytometry analysis and quantitative data of matured DCs ($CD45^+$ $CD11c^+$ $CD86^+$) in lymph nodes after various treatments. i–k)

$PDI(Br)_6$ NPs, the antitumor performance in *vivo* was investigated against 4T1 tumor-bearing mice (**Figure 6a**). The phototherapy was conducted followed by 808 nm laser irradiation at 12 h post-injection of $PDI(Br)_6$ NPs and PBS as control. The tumor volumes and body weights of the mice were monitored after various treatments. Compared to PBS or PBS + laser treatment groups, the $PDI(Br)_6$ NPs treatment group delayed tumor proliferation effects, suggesting that $[PDI(Br)_6]$ $NPs^{\bullet-}$ were specifically produced in tumors with chemodynamic ROS generation. By sharp contrast, the group treated with $PDI(Br)_6$ NPs + laser displayed significant tumor suppression, indicating Type-I PDT and CDT combination therapy could effectively inhibit tumor growth (Figure 6b; Figure S66, Supporting Information). A similar tendency was also observed in the weight of tumors after treatment (Figure 6c). In addition, by comparing the PBS or PBS+laser treatment groups, it was found that spleen size was significantly downregulated in both $PDI(Br)_6$ NPs and $PDI(Br)_6$ NPs + laser groups (Figure 6d). The body weights of all treated mice showed no significant changes throughout the treatment process (Figure 6e). Furthermore, major organs such as the heart, liver, spleen, lung, and kidney showed no alterations post-treatment (Figure S67, Supporting Information). The basic blood parameters remained within a reasonable range post-treatment (Figure S68, Supporting Information). These findings indicated that the tumor-specific activated $[PDI(Br)_6]$ $NPs^{\bullet-}$ owning favorable biocompatibility and biosafety in the treatment. After treatment, we conducted hematoxylin and eosin (H&E) staining, TUNEL staining, and Ki67 staining analyses to verify the in vivo phototherapeutic mechanism of $PDI(Br)_6$ NPs (Figure 6f). The H&E assay exhibited the extensive destruction of tumor tissues in the therapeutic groups of $PDI(Br)_6$ NPs and $PDI(Br)_6$ NPs + laser. In contrast, the tumor cells remained a vibrant and dense arrangement in the control groups. The severe apoptosis of $PDI(Br)_6$ NPs and $PDI(Br)_6$ NPs + laser groups was proved by TUNEL staining. Meanwhile, the inhibited vessel formation and suppressed cell proliferation of the tumor region were further confirmed according to the Ki67 staining. These outcomes solidly manifested that the collaborative Type-I PDT and CDT could afford effective therapeutic efficiency.

Mature dendritic cells (DCs) are essential antigen-presenting cells in antitumor immune responses, playing a critical role in activating $CD8^+$ cytotoxic T lymphocytes (CTLs) to effectively suppress metastatic tumors. As we mentioned that the burst release of ROS by Type-I PDT and CDT combination therapy could elicit ICD and prime antitumor immune responses, thus, we first examined the maturation of dendritic cells (DCs) in the treated mice. The relative content of mature DCs ($CD45^+CD11c^+CD86^+$) was significantly high at 25% in the $PDI(Br)_6$ NPs+laser group compared to 9.55% in the PBS group, 16.9% in the $PDI(Br)_6$ NPs group, and 12% in the PBS + laser group (Figure 6g,h), suggesting the ROS-triggered ICD effect could enhance DC maturation. CTLs ($CD3^+CD8^+$ T cells) and helper T cells ($CD3^+CD4^+$ T cells) are essential to against cancer cells, triggering an adaptive immune response. As a result, $PDI(Br)_6$ NPs+laser treated tumor showed an increase in recruitment of $CD3^+CD4^+$ T cells into the tumor by 29.9%, which was 1.88, 1.68, and 1.46-fold higher than the PBS (15.9%), PBS + laser (17.7%), and $PDI(Br)_6$ NPs (20.4%) groups (Figure 6i–k). Similar results showed the recruitment of $CD3^+CD8^+$ T cells into the tumors. Furthermore, compared with PBS and PBS+laser, $PDI(Br)_6$ NPs and $PDI(Br)_6$ NPs+laser showed high levels of HMGB1 expression and infiltration of $CD8^+$ T cells, presenting solid evidence for the $PDI(Br)_6$ NPs-triggered antitumor immune response (Figure 6l). We then assessed systemic immune responses by measuring serum levels of pro-inflammatory cytokines including interleukin 6 (IL-6), interleukin 1β (IL-1β), tumor necrosis factor-alpha (TNF-α), and interferon-gamma (IFN-γ). The ELISA assay showed a significant increase in IL-6 and IL-1β levels in the serum of mice treated with $PDI(Br)_6$ NPs and $PDI(Br)_6$ NPs + laser compared to control groups (PBS, PBS + laser), indicating a strong antitumor immune response in the experimental groups. Additionally, TNF-α and IFN-γ levels were notably elevated after treatment with $PDI(Br)_6$ NPs or $PDI(Br)_6$ NPs+laser on mice (Figure 6m–p). All the results suggested that the tumor-specific activated $[PDI(Br)_6]$ $NPs^{\bullet-}$ mediated tumor chemo/photodynamic combination therapy followed with initiating antitumor immune response and low side-effect.

3. Conclusion

In summary, we obtain the four kinds of $PDI(Br)_{0/2/4/6}$ and prepare the corresponding water-soluble $PDI(Br)_{0/2/4/6}$ NPs via nanoprecipitation. ESR spectroscopy and DFT-calculated results have confirmed their open-shell ground states, and comparative studies have further demonstrated that variations in the number of Br substituents on the PDI skeleton significantly influence the optical and ROS properties of the PDI SORs. Quantum chemical calculations and fs-TA spectra are further performed to demonstrate an increase of Br atoms on the PDI skeleton effectively reduces intermolecular π–π stacking energy and improves the electron transfer rate, enhancing excited-state charge transfer characteristics. $[PDI(Br)_6]$ $NPs^{\bullet-}$ are specifically activated in hypoxic tumors exhibiting high stability, strong PA and NIR-II fluorescence signals. The generated $[PDI(Br)_6]$ $NPs^{\bullet-}$ show chemodynamic and photodynamic properties for eliciting a strong tumor ICD effect and exhibiting systematical safety. This study offers tumor-specific activatable PDI SORs for "turn on" tumor theranostics, and provides new insights for developing new SORs for precision medicine.

Representative flow cytometry analysis and quantitative data of the percentages of T cells ($CD3^+CD4^+$ and $CD3^+CD8^+$) were collected after various treatments. Data are presented as mean ± SD (n = 3 mice). l) Representative $CD8^+$, HMGB1 staining of tumor sections harvested from the mice receiving different treatments. Scale bars: 100 µm. Quantification of systemic cytokines within the mice serum. m) serum TNF-α levels, n) serum IFN-γ levels, o) serum IL-1β levels, p) serum IL-6 levels were analyzed by enzyme-linked immunosorbent assay (ELISA). Data are presented as mean ± SD (n = 3 mice). GI: PBS, GII: $PDI(Br)_6$ NPs, GIII: PBS + laser, GIV: $PDI(Br)_6$ NPs + laser. Data are presented as means ± s.d. Statistical significance was calculated via One-way ANOVA with Tukey post-hoc test. $^*P < 0.05$, $^{**}P < 0.01$, $^{***}P < 0.001$ and $^{****}P < 0.0001$.

Supporting Information

Supporting Information is available from the Wiley Online Library or from the author.

Acknowledgements

J.Z. and H.F.L. contributed equally to this work. This work was financially supported by the National Natural Science Foundation of China (82302356, 32360236), the Hainan Provincial Natural Science Foundation of China (123MS001), Joint Funds for the Innovation of Science and Technology, Fujian province (2023Y9320), Fujian Province Natural Science Fund Project (2024J011105), National Key R&D Program of China (2023YFC2413500), Innovation team of Photoelectric functional materials and devices for biomedical theranostics of Fujian Normal University (Y07204080K13), Sponsored by Fujian Provincial Health Technology Project (Grant No. 2024ZD01004), the Natural Science Foundation of Fujian Province (2023J01529), The animal experiment procedures were conducted following an approved protocol (IACUC-20230045) by Fujian Normal University Animal Ethics Committee.

Conflict of Interest

The authors declare no conflict of interest.

Data Availability Statement

The data that support the findings of this study are available from the corresponding author upon reasonable request.

Keywords

CDT, immunotherapy, NIR-II FLI, semiconducting open-shell radicals, tumor activatable phototheranostics, type-I PDT

Received: January 9, 2025
Revised: February 12, 2025
Published online: March 7, 2025

[1] D. O. Lopez-Cantu, R. B. González-González, A. Sharma, M. Bilal, R. Parra-Saldívar, H. M. Iqbal, *Coord. Chem. Rev.* **2022**, *469*, 214685.
[2] D. Chuan, H. Hou, Y. Wang, M. Mu, J. Li, Y. Ren, N. Zhao, B. Han, H. Chen, G. Guo, *J. Mater. Sci. Technol.* **2023**, *152*, 159.
[3] D. Jiang, D. Ni, Z. T. Rosenkrans, P. Huang, X. Yan, W. Cai, *Chem. Soc. Rev.* **2019**, *48*, 3683.
[4] T. Wang, C. Ménard-Moyon, A. Bianco, *Chem. Soc. Rev.* **2022**, *51*, 3535.
[5] L. T. Huang, Z. J. Chen, Z. Yang, W. Huang, *BME Front* **2024**, *5*, 0062.
[6] S. He, P. Cheng, K. Pu, *Nat. Biomed. Eng.* **2023**, *7*, 281.
[7] Y. X. Hu, J. Yu, M. K. Xu, K. Pu, *J. Am. Chem. Soc.* **2024**, *146*, 12656.
[8] L. K. B. Tam, J. C. H. Chu, L. He, C. Yang, K. C. Han, P. C. K. Cheung, D. K. P. Ng, P. C. Lo, *J. Am. Chem. Soc.* **2023**, *145*, 7361.
[9] J. L. Kolanowski, F. Liu, E. J. New, *Chem. Soc. Rev.* **2018**, *47*, 195.
[10] J. S. Wu, J. Sha, C. L. Zhang, W. M. Liu, X. L. Zheng, P. F. Wang, *VIEW* **2020**, *1*, 20200090.
[11] J. D. Knoll, B. A. Albani, C. Turro, *Acc. Chem. Res.* **2015**, *48*, 2280.
[12] X. Qin, C. Wu, D. C. Niu, L. M. Qin, X. Wang, Q. G. Wang, Y. S. Li, *Nat. Commun.* **2021**, *12*, 5243.
[13] G. Z. Zhou, M. Li, *Adv. Mater.* **2022**, *34*, 2200871.
[14] X. Y. Kang, Y. Zhang, J. W. Song, L. Wang, W. Li, J. Qi, B. Z. Tang, *Nat. Commun.* **2023**, *14*, 5216.
[15] P. L. Cen, J. N. Huang, C. T. Jin, J. Wang, Y. Wei, H. Zhang, M. Tian, *Aggregate* **2023**, *4*, e298.
[16] J. S. Huang, L. C. Su, C. Xu, X. G. Ge, R. P. Zhang, J. B. Song, K. Pu, *Nat. Mater.* **2023**, *22*, 1421.
[17] J. Huang, Y. Jiang, J. Li, S. He, J. Huang, K. Pu, *Angew. Chem., Int. Ed.* **2020**, *59*, 4415.
[18] X. Wang, S. He, P. Cheng, K. Pu, *Adv. Mater.* **2023**, *35*, 2206510.
[19] M. Bertolini, M. S. Wong, L. Mendive-Tapia, M. Vendrell, *Chem. Soc. Rev.* **2023**, *52*, 5352.
[20] P. Cheng, S. He, C. Zhang, J. Liu, K. Pu, *Angew. Chem., Int. Ed.* **2023**, *135*, e202301625.
[21] Y. Y. Zhao, L. Zhang, Z. X. Chen, B. Y. Zheng, M. R. Ke, X. S. Li, J. D. Huang, *J. Am. Chem. Soc.* **2021**, *143*, 13980.
[22] M. L. Li, T. Xiong, J. J. Du, R. S. Tian, M. Xiao, L. Y. Guo, S. R. Long, J. L. Fan, W. Sun, K. Shao, X. Z. Song, J. W. Foley, X. J. Peng, *J. Am. Chem. Soc.* **2019**, *141*, 2695.
[23] Y. Y. Wang, Y. C. Liu, H. Sun, D. S. Guo, *Coord. Chem. Rev.* **2019**, *395*, 46.
[24] X. Li, N. Kwon, T. Guo, Z. Liu, J. Yoon, *Angew. Chem., Int. Ed.* **2018**, *57*, 11522.
[25] L. M. Loftus, A. Li, K. L. Fillman, P. D. Martin, J. J. Kodanko, C. Turro, *J. Am. Chem. Soc.* **2017**, *139*, 18295.
[26] C. Zhang, C. Ye, J. N. Yao, L. Z. Wu, *Nat. Sci. Rev.* **2024**, *11*, 244.
[27] X. Q. Zhao, J. Y. Gong, P. Alam, C. Ma, Y. P. Wang, J. Guo, Z. B. Zeng, Z. K. He, H. H. Y. Sung, I. Williams, K. S. Wong, S. J. Chen, J. W. Y. Lam, Z. Zhao, B. Z. Tang, *CCS Chem* **2022**, *4*, 1912.
[28] S. F. Nelsen, *J. Am. Chem. Soc.* **1967**, *89*, 5925.
[29] M. Al Kobaisi, S. V. Bhosale, K. Latham, A. M. Raynor, S. V. Bhosale, *Chem. Rev.* **2016**, *116*, 11685.
[30] Z. B. Zhou, K. Yang, L. He, W. Wang, W. M. Lai, Y. H. Yang, Y. G. Dong, S. Xie, L. Yuan, Z. B. Zeng, *J. Am. Chem. Soc.* **2024**, *146*, 6763.
[31] L. Feng, Y. Y. Tuo, Z. P. Wu, W. J. Zhang, C. B. Li, B. Yang, L. X. Liu, J. Y. Gong, G. Y. Jiang, W. Hu, B. Z. Tang, L. M. Wu, J. G. Wang, *J. Am. Chem. Soc.* **2024**, *146*, 32582.
[32] N. Moriyama, J. Abe, *J. Am. Chem. Soc.* **2023**, *145*, 3318.
[33] D. Schmidt, D. Bialas, F. Wrthner, *Angew. Chem., Int. Ed.* **2015**, *54*, 3611.
[34] T. Y. Jiao, K. Cai, J. N. Nelson, Y. Jiao, Y. Y. Qiu, G. C. Wu, J. W. Zhou, C. Y. Cheng, D. K. Shen, Y. M. Feng, Z. C. Liu, M. R. Wasielewski, J. F. Stoddart, H. Li, *J. Am. Chem. Soc.* **2019**, *141*, 16915.
[35] T. He, M. Stolte, F. Wurthner, *Adv. Mater.* **2013**, *25*, 6951.
[36] S. Guha, S. Saha, *J. Am. Chem. Soc.* **2010**, *132*, 17674.
[37] Z. Mi, P. Yang, R. Wang, J. Unruangsri, W. Yang, C. Wang, J. Guo, *J. Am. Chem. Soc.* **2019**, *141*, 14433.
[38] B. Tang, W. L. Li, Y. Chang, B. Yuan, Y. Wu, M. T. Zhang, J. F. Xu, J. Li, X. Zhang, *Angew. Chem., Int. Ed.* **2019**, *58*, 15526.
[39] I. Ghosh, T. Ghosh, J. I. Bardagi, B. König, *Science* **2014**, *346*, 725.
[40] P. Ravat, T. Solomek, D. Haussinger, O. Blacque, M. Juricek, *J. Am. Chem. Soc.* **2018**, *140*, 10839.
[41] T. J. Whittemore, A. Millet, H. J. Sayre, B. S. Dolinar, E. G. White, K. R. Dunbar, C. Turro, *J. Am. Chem. Soc.* **2018**, *140*, 5161.
[42] G. E. Rudebusch, J. L. Zafra, K. Jorner, K. Fukuda, J. L. Marshall, I. Arrechea-Marcos, G. L. Espejo, R. P. Ortiz, C. J. Gomez-Garcia, L. N. Zakharov, M. Nakano, H. Ottosson, J. Casado, M. M. Haley, *Nat. Chem.* **2016**, *8*, 753.
[43] H. Gao, X. Zhi, F. Wu, Y. Zhao, F. Cai, P. Li, Z. Shen, *Angew. Chem., Int. Ed.* **2023**, *62*, e202309208.
[44] R. Englman, J. Jortner, *Mol. Phys.* **1970**, *18*, 145.
[45] X. Cui, G. Lu, S. Dong, S. Li, Y. Xiao, J. Zhang, Y. Liu, X. Meng, F. Li, C. S. Lee, *Mater. Horiz.* **2021**, *8*, 571.
[46] B. B. Zhang, R. J. Zheng, Y. T. Liu, X. Lou, W. Zhang, Z. J. Cui, Y. W. Huang, T. Wang, *Adv. Sci.* **2022**, *10*, 2204498.

[47] X. Lou, H. Wang, Y. Liu, Y. W. Huang, Z. H. Liu, W. Zhang, T. Wang, *Angew. Chem., Int. Ed.* **2023**, *62*, e202214586.
[48] J. Zhang, W. Ma, H. F. Luo, K. X. Zhang, J. Q. Lv, L. Z. Jiang, Y. L. Huang, J. B. Song, Z. Yang, W. Huang, *Adv. Healthcare Mater.* **2024**, *13*, 2303175.
[49] Y. Kumar, S. Kumar, K. Mandal, P. Mukhopadhyay, *Angew. Chem., Int. Ed.* **2018**, *57*, 16318.
[50] H. C. Mao, G. J. Pazera, R. M. Young, M. D. Krzyaniak, M. R. Wasielewski, *J. Am. Chem. Soc.* **2023**, *145*, 6585.
[51] Y. L. Wu, N. E. Horwitz, K. S. Chen, D. A. Gomez-Gualdron, N. S. Luu, L. Ma, T. C. Wang, M. C. Hersam, J. T. Hupp, O. K. Farha, R. Q. Snurr, M. R. Wasielewski, *Nat. Chem.* **2016**, *9*, 466.
[52] L. Zeng, L. Huang, Z. Huang, T. Mani, K. Huang, C. Y. Duan, G. Han, *Nat. Commun.* **2024**, *15*, 7270.
[53] Y. Jiao, K. Liu, G. T. Wang, Y. P. Wang, X. Zhang, *Chem. Sci.* **2015**, *6*, 3975.
[54] Y. F. Wu, S. W. Ying, L. Y. Su, J. J. Du, L. Zhang, B. W. Chen, H. R. Tian, H. Xu, M. L. Zhang, X. Yan, *J. Am. Chem. Soc.* **2022**, *144*, 10736.
[55] C. J. Zeman, S. J. Kim, F. Zhang, K. S. Schanze, *J. Am. Chem. Soc.* **2020**, *142*, 2204.
[56] K. Zhou, L. L. Du, R. Ding, L. T. Xu, S. Shi, S. Y. Wang, Z. Y. Wang, G. Q. Zhang, G. He, Z. Zhao, B. Z. Tang, *Nat Commun.* **2024**, *15*, 10551.
[57] Z. J. Zhao, F. S. Niu, P. J. Li, H. Q. Wang, Z. H. Zhang, G. J. Meyer, K. Hu, *J. Am. Chem. Soc.* **2022**, *144*, 7043.
[58] X. M. Hu, Z. T. Fang, F. W. Sun, C. J. Zhu, M. Y. Jia, X. F. Miao, L. T. Huang, W. B. Hu, Q. L. Fan, Z. Yang, W. Huang, *Angew. Chem., Int. Ed.* **2024**, *63*, e202401036.
[59] X. Miao, W. B. Hu, T. He, H. Tao, Q. Wang, R. Chen, L. Jin, H. Zhao, X. Lu, Q. L. Fan, W. Huang, *Chem. Sci.* **2019**, *10*, 3096.
[60] H. Wang, K. F. Xue, Y. C. Yang, H. Hu, F. J. Xu, X. Zhang, *J. Am. Chem. Soc.* **2022**, *144*, 2360.
[61] L. Zhao, Y. Liu, R. Xing, X. Yan, *Angew. Chem., Int. Ed.* **2020**, *59*, 3793.
[62] X. J. Zhao, R. J. Zheng, B. B. Zhang, Y. Zhao, W. L. Xue, Y. F. Fang, Y. W. Huang, M. Z. Yin, *Angew. Chem., Int. Ed.* **2024**, *136*, e202318799.
[63] C. Ji, Q. Gao, X. Dong, W. Yin, Z. Gu, Z. Gan, Y. Zhao, M. Z. Yin, *Angew. Chem., Int. Ed.* **2018**, *57*, 11384.
[64] J. Zhao, W. Wu, J. Sun, S. Guo, *Chem. Soc. Rev.* **2013**, *42*, 5323.
[65] S. M. Dyar, E. A. Margulies, N. E. Horwitz, K. E. Brown, M. D. Krzyaniak, M. R. Wasielewski, *J. Phys. Chem. B* **2015**, *119*, 13560.
[66] R. Lincoln, L. Kohler, S. M. A. Monro, H. M. Yin, M. Stephenson, R. Zong, A. Chouai, C. L. Dorsey, R. A. Hennigar, R. S. M. Thummel, *J. Am. Chem. Soc.* **2013**, *135*, 17161.
[67] K. Ishii, Y. Hirose, H. Fujitsuka, O. Ito, N. Kobayashi, *J. Am. Chem. Soc.* **2001**, *123*, 702.
[68] C. Michael T, G. Emilie M, C. Boiko, M. Tomoaki, S. Amy M, W. Michael R, *J. Phys. Chem. A* **2010**, *114*, 1741.
[69] Y. Teki, S. Miyamoto, K. Iimura, M. Nakatsuji, Y. Miura, *J. Am. Chem. Soc.* **2000**, *122*, 984.